Electronic structure, spin-orbit coupling, and interlayer interaction in bulk MoS_2 and WS_2

Drew W. Latzke,[1,2] Wentao Zhang,[2,3] Aslihan Suslu,[4] Tay-Rong Chang,[5] Hsin Lin,[6,7] Horng-Tay Jeng,[5,8] Sefaattin Tongay,[4] Junqiao Wu,[2,9] Arun Bansil,[10] and Alessandra Lanzara[2,3,*]

[1] *Applied Science & Technology, University of California, Berkeley, California 94720, USA*
[2] *Materials Sciences Division, Lawrence Berkeley National Laboratory, Berkeley, California 94720, USA*
[3] *Department of Physics, University of California, Berkeley, California 94720, USA*
[4] *School for Engineering of Matter, Transport and Energy, Arizona State University, Tempe, AZ 85287, USA*
[5] *Department of Physics, National Tsing Hua University, Hsinchu 30013, Taiwan*
[6] *Centre for Advanced 2D Materials and Graphene Research Centre, National University of Singapore, Singapore 117546*
[7] *Department of Physics, National University of Singapore, Singapore 117542*
[8] *Institute of Physics, Academia Sinica, Taipei 11529, Taiwan*
[9] *Department of Materials Science and Engineering, University of California, Berkeley, California 94720, USA*
[10] *Department of Physics, Northeastern University, Boston, Massachusetts 02115, USA*

(Dated: October 8, 2015)

We present in-depth measurements of the electronic band structure of the transition metal dichalcogenides (TMDs) MoS_2 and WS_2 using angle-resolved photoemission spectroscopy, with focus on the energy splittings in their valence bands at the K point of the Brillouin zone. Experimental results are interpreted in terms of our parallel first-principles computations. We find that interlayer interaction only weakly contributes to the splitting in bulk WS_2, resolving previous debates on its relative strength. We additionally find that across a range of TMDs, the band gap generally decreases with increasing magnitude of the valence band splitting, molecular mass, or ratio of the out-of-plane to in-plane lattice constant. Our results provide an important reference for future studies of electronic properties of MoS_2 and WS_2, and their applications in spintronics and valleytronics devices.

I. INTRODUCTION

Transition metal dichalcogenides (TMDs) (MX_2 where M = Mo or W and X = S, Se, or Te) are layered semiconducting materials that have recently shown promise for application to a wide range of electronic devices, including the growing fields of spintronics and valleytronics[1]. In the monolayer limit, TMDs are theorized to have a split valence band that is nearly fully spin polarized[2] near the K and K′ points of the hexagonal Brillouin zone. The spin polarization is predicted to be reversed between the K and K′ points, implying existence of an unusual spin-valley coupling in the TMDs. The ability to selectively populate[3–5] these valleys demonstrates their viability for use in spintronics/valleytronics devices.

Despite the importance of the split valence band that governs the unique spin and valley physics of TMDs, there remain questions regarding the origin of these splittings in bulk TMDs. In particular, this splitting is theorized to be entirely a consequence of spin-orbit coupling in the monolayer limit, and a combination of spin-orbit coupling and interlayer interaction in the bulk limit, but there is disagreement[6–9] about the relative strength of the two mechanisms in the bulk limit. Current electronic band structure studies of bulk MoS_2[9–14] and WS_2[6] are limited by energy and momentum resolution and lack focus on the valence band splittings. Experimentally, the sizes of the splittings have been characterized, but only with limited resolution.

Here we present high-resolution angle-resolved photoemission spectroscopy (ARPES) data of the electronic band structure of bulk MoS_2 and WS_2, and analyze our measurements via parallel first-principles computations. Our findings resolve previous debates on the role of interlayer interaction on the valence band splitting, revealing that the splitting in the bulk samples is primarily due to spin-orbit coupling and not interlayer interaction. In order to gain insight into the nature of this splitting, we further investigate its origins, its magnitude, and its correlation with the electronic band gap across a range of TMDs. Our comparisons for various TMDs reveal the interplay between the valence band splitting, band gap, molecular mass, and out-of-plane to in-plane lattice constant ratio, suggesting how specific TMDs would be suited for particular applications.

II. METHODS

High-resolution ARPES experiments on MoS_2 (WS_2) were performed at Beamline 10.0.1.1 (4.0.3) of the Advanced Light Source at a temperature of 150 K using 50 eV (52-120 eV) photons. The total energy resolution was 10 meV (20 meV) for experiments on MoS_2 (WS_2) with an angular resolution ($\Delta\theta$) of $\leq 0.2°$. The momentum resolution ($\Delta k_{\parallel}$) is related to the angular resolution

by $\Delta k_{\parallel} \simeq \sqrt{2mE_k/\hbar^2} \cdot \cos\theta \cdot \Delta\theta$ where the kinetic energy of the ejected electrons (E_k) is dependent on the incident photon energy[15]. The samples were cleaved in situ at 150 K in a vacuum better than 5×10^{-11} Torr.

The electronic structures of MX_2 (M = Mo or W and X = S, Se, or Te) were computed using the projector augmented wave method[16,17] as implemented in the VASP[18–20] package within the generalized gradient approximation (GGA)[21] scheme. A $15 \times 15 \times 3$ Monkhorst-Pack k-point mesh was used in the computations. We used experimental lattice constants and relaxed the atomic positions until the residual forces were less than 0.001 eV/Å. The spin-orbit coupling effects were included self-consistently. In order to correct the energy band gaps, we also performed calculations with the HSE hybrid functional[22,23].

Single crystals were synthesized using the Br_2 vapor transport technique in a two-zone furnace system. Mo, W, and S powders (purity 99.9995%) were mixed in stoichiometric ratios in a sealed quartz tube at 1×10^{-7} Torr pressure and annealed to 880 °C for one week to yield precursor powders. Next, they were loaded into 2 inch diameter tubes with Br_2 liquid, pumped down to 1×10^{-7} Torr, and sealed. Typical growth parameters were established as heat up for one week from room temperature to 910 °C, the low temperature zone was set to 890 °C in one day, and the system was kept at this temperature for three weeks and controllably cooled down to room temperature in one week. Synthesized crystals displayed strong Raman signals at 384 cm^{-1} and 407 cm^{-1} for MoS_2, and 352 cm^{-1} and 417 cm^{-1} for WS_2. Lastly, monolayers exfoliated from MoS_2 and WS_2 crystals displayed sharp bright luminescence peaks at 1.88 eV and 2.04 eV, respectively.

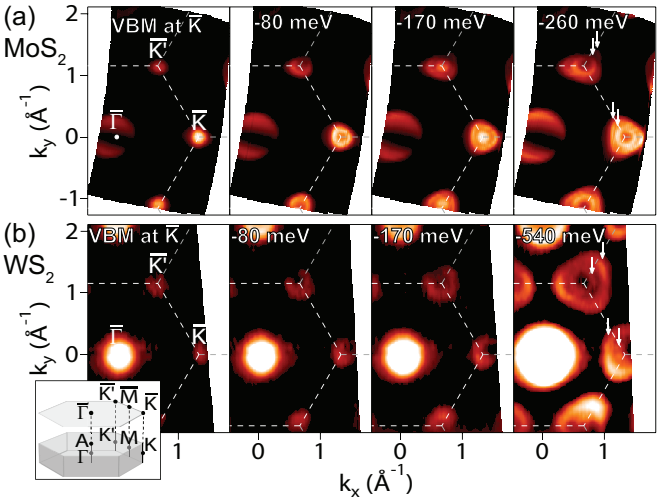

FIG. 1. Constant energy maps of the electronic band structure of bulk **(a)** MoS_2 and **(b)** WS_2 taken at photon energies of 50 eV and 90 eV, respectively. The maps were taken at and below the energy corresponding to their respective valence band maximum (VBM) at $\overline{\mathrm{K}}$. The dashed white line indicates the two-dimensional (reduced in the k_z dimension as shown in the inset) hexagonal Brillouin zone. Evolution of the valence band with increase in binding energy about the $\overline{\Gamma}$, $\overline{\mathrm{K}}$, and $\overline{\mathrm{K}'}$ points can be observed for both samples. An energy splitting at the $\overline{\mathrm{K}}$ and $\overline{\mathrm{K}'}$ points can be observed in the MoS_2 maps, most easily at 170 meV or 260 meV below the VBM (white arrows). The splitting for WS_2 is not observed 170 meV below the VBM, but can be observed 540 meV below the VBM (white arrows). Trigonal warping of the valence band about the $\overline{\mathrm{K}}$ and $\overline{\mathrm{K}'}$ points can be observed for both samples.

III. RESULTS AND DISCUSSION

A. Characterizing the Origins of the Splitting

Fig. 1(a) and 1(b) show detailed momentum-resolved constant-energy maps for bulk MoS_2 and WS_2, respectively. The two-dimensional (reduced in the k_z dimension as shown in the inset) hexagonal Brillouin zone is overlaid as white dashed lines. The observed suppression of intensity in MoS_2 along a specific momentum direction near $\overline{\Gamma}$ is due presumably to matrix element effects[24]. The evolution of the valence band about the $\overline{\Gamma}$, $\overline{\mathrm{K}}$, and $\overline{\mathrm{K}'}$ points can be clearly observed throughout the range of binding energies shown. We offset the two sets of data so that the valence band maximum at $\overline{\mathrm{K}}$ is shown at the same energy and we compare the two band structures as binding energy is increased. The two samples produce similar spectra with the most notable difference being the appearance of the lower split valence band at $\overline{\mathrm{K}}$ at approximately 170 meV below the local valence band maximum (VBM) for MoS_2. This appears as a small circular feature centered at $\overline{\mathrm{K}}$ within a larger concentric feature. The analogous splitting for WS_2 becomes apparent in the spectra at much higher binding energy, as seen in the map at 540 meV below the VBM. The splitting for both samples is shown by vertical white arrows. Trigonal warping of the valence band in the vicinity of the $\overline{\mathrm{K}}$ and $\overline{\mathrm{K}'}$ points, similar to that seen in other bulk TMDs[8,14], is observed for both samples and presented here for the first time for bulk WS_2. This deviation from a circular feature about $\overline{\mathrm{K}}$ and $\overline{\mathrm{K}'}$ is more pronounced at higher binding energies where the feature becomes more triangular. An analogous trigonal warping has been predicted[25,26] to occur in monolayer MoS_2 samples as a consequence of the orbital structure of these bands and anisotropic (order q^3) corrections to the energy but has not been observed so far in an ARPES experiment.

To obtain information about the k_z dispersion, i.e. the interlayer dispersion, in Figure 2(a) we show detailed photon energy dependent maps compared with k_z-resolved theoretical calculations of bulk WS_2 along the $\overline{\Gamma}$–$\overline{\mathrm{K}}$ high symmetry direction. Indeed, at normal emission ($k_{\parallel} = 0$), k_z is related to the kinetic energy of the ejected electrons (E_k) by $k_z = \sqrt{2m(E_k + V_{in})/\hbar^2}$ where V_{in} is the inner potential determined from the

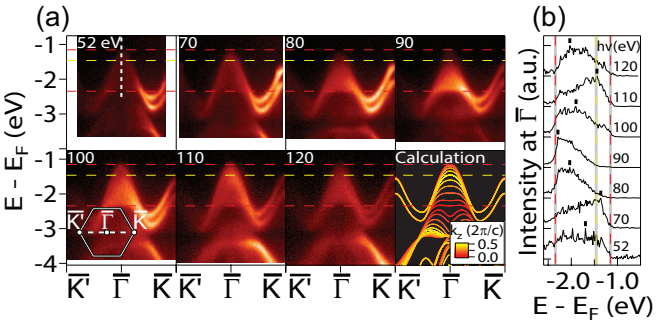

FIG. 2. **(a)** Photon energy dependence from 52 to 120 eV and theoretical calculations of the electronic band structure of bulk WS_2 along the $\overline{\Gamma}$–$\overline{K}$ high symmetry direction. The horizontal red (yellow) dashed lines correspond to the calculated location of bulk WS_2 bands at the Γ point (A point). Observed intensity shifts of the valence band near the $\overline{\Gamma}$ point at different binding energies is evidence of strong k_z dispersion. **(b)** Energy distribution curves (EDCs) (solid black lines) taken along $k_x = k_y = 0$ Å^{-1} of the respective maps in (a) (e.g. along the white dashed line in the 52 eV map). The vertical red (yellow) dashed lines correspond to the calculated location of bulk WS_2 bands at the Γ point (A point). The peak in intensity (denoted by the tick marks) shifts periodically between higher and lower binding energies as a result of the strong k_z dispersion. Peaks in the 70 eV and 110 eV EDCs as well as the top of the feature in the 90 eV EDC correspond to the theoretical band maximum at A.

measured dispersion[27,28]. Near $\overline{\Gamma}$, we observe a broad feature likely associated with the convolution of the various bands predicted for different k_z values as it extends between the two horizontal red dashed lines corresponding to the calculated energies of the top two valence bands at Γ ($k_z = 0$). The top of this broad feature aligns well with the calculated valence band maximum at Γ ($k_z = 0$) for the 52 eV map and as the photon energy is increased further, the top of the feature decreases in energy until it aligns with the calculated valence band maximum at the A point ($k_x = k_y = 0$, $k_z = \frac{\pi}{c}$) indicated by the horizontal yellow dashed line in the 90 eV map. Increasing the photon energy further returns the top of the valence band feature to its maximum value.

The observed k_z dispersion at $\overline{\Gamma}$ is investigated more closely in Fig. 2(b) by comparing energy distribution curves (EDCs) taken at $\overline{\Gamma}$ for each of the incident photon energies (e.g. along the dashed white line in the 52 eV image in (a)). The observation of a large spread in energy of the main peak in the EDC spectra between the calculated energies of the top two valence bands at Γ (vertical red dashed lines) is in agreement with the association of the broad feature near $\overline{\Gamma}$ with the convolution of multiple bands predicted for different k_z values. The peak intensity (tick mark) moves up and down in binding energy in a periodic manner confirming the strong k_z dependence of these bands. Overall, our observed k_z dispersions agree well with other predictions for WS_2[6] and our calculations which predict wide variation in binding energy (up to 880 meV) of the bands as k_z changes from 0 to $\frac{\pi}{c}$. Similar k_z dispersions are also found theoretically and experimentally more generally in TMDs[29–32].

Near $\overline{K}$, we observe the band splitting at the top of the valence bands for all photon energies, indicating that the splitting occurs for all corresponding k_z values. We measure the magnitude of the splitting to vary between 414 meV and 441 meV in accordance with our corresponding predicted range of 410 meV ($k_z = \frac{\pi}{c}$) to 466 meV ($k_z = 0$). This relatively small change in magnitude of the splitting (27 meV experimentally and 56 meV theoretically) across this range of photon energies indicates weak k_z dispersion near $\overline{K}$ and $\overline{K'}$. This is in contrast to the observation of large variations in the spectra of the broad feature at $\overline{\Gamma}$ which indicates strong k_z dispersion of the bands near $\overline{\Gamma}$.

As a result of the layered structure of bulk TMDs, the three-dimensional character of the band structure is directly related to the strength of the interlayer interaction. The strong k_z dispersion at $\overline{\Gamma}$ is a reflection of the three-dimensional character of those bands. However, the relatively weak k_z dispersion at $\overline{K}$ and $\overline{K'}$ is a reflection of the two-dimensional character of those bands and shows that interlayer interaction has a weak effect on the valence band splitting. Hence, we conclude that the splitting is dominated by spin-orbit coupling with interlayer interaction playing a minor role.

B. The Effect of Spin-Orbit Coupling on the Valence Band Structure

Figure 3 shows high-resolution energy versus momentum maps of the band structure of bulk MoS_2 (panel a) and WS_2 (panel b). Band dispersions can be seen as far as 8 eV below the Fermi energy; many of these bands have not been observed before. The experimental band structure shows remarkable agreement with our theoretical predictions (blue dashed lines) throughout this energy and momentum region. The intensity of the valence band maximum near $\overline{\Gamma}$ for MoS_2 is reduced due presumably to matrix element effects[24]. Additionally, intensity of the experimental bands with low binding energy may be shifted near $\overline{\Gamma}$ due to their strong k_z dependence (as shown for WS_2 in Fig. 2). The splitting of the valence band at $\overline{K}$ is fully resolved for both samples (as indicated by the white arrows) and is found to be 170 ± 2 meV for MoS_2 and 425 ± 18 meV for WS_2 (as shown in the upper insets). The value for MoS_2 agrees well with our experimental constant energy maps presented in Fig. 1(a) as the lower split band for MoS_2 appears 170 meV below the higher split band. The value for WS_2 is consistent with our experimental constant energy maps in Fig. 1(b) as the lower split band is not visible 170 meV below the higher split band, but is clearly visible 540 meV below. These measured magnitudes are smaller by approximately 100 meV than the values of 265 meV for MoS_2 and 570 meV for WS_2 predicted by HSE-based calcula-

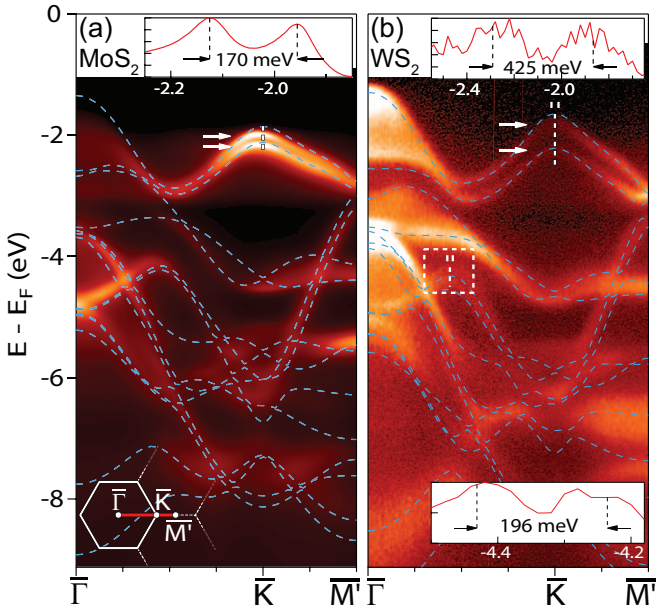

FIG. 3. High resolution maps of the electronic band structure of bulk **(a)** MoS_2 and **(b)** WS_2 along the $\overline{\Gamma}$–$\overline{K}$ high symmetry direction with theoretical calculations overlaid as dashed blue lines. Spin-orbit coupling and interlayer interaction induced splitting in the valence band near the $\overline{K}$ point is fully resolved for both samples as indicated by the white arrows and the respective EDCs (upper insets) taken along the upper white dashed lines. [Here the WS_2 EDC was integrated in momentum between the two white tick marks.] The splitting is found to be approximately 170 ± 2 meV for MoS_2 and 425 ± 18 meV for WS_2. An additional splitting in a higher binding energy WS_2 valence band is observed within the white dashed rectangle in panel (b). The lower inset presents an EDC taken along the vertical white dashed line corresponding to the energy and momentum location of the maximum splitting of 196 ± 22 meV. [Here the EDC was integrated in momentum between the two white tick marks and smoothed with a Savitzky-Golay filter.] The calculated band structure is found to be in excellent agreement with the experimental band structure for both samples. The discrepancy in the location of the valence band near the $\overline{\Gamma}$ point for bulk MoS_2 can be attributed to its strong k_z dispersion.

tions. However, our experimental values agree very well with GGA-based calculations that predict a splitting of 145-224 meV for MoS_2 and 410-466 meV for WS_2 across all k_z values. The large difference in magnitude between the splittings for MoS_2 and WS_2 can be explained by the larger intrinsic spin-orbit coupling of tungsten compared with that of molybdenum. Additionally, our calculations predict a substantial splitting of a valence band of WS_2 at high binding energy (see white dashed rectangle). The maximum splitting predicted is in agreement with the experimental value of 196 ± 22 meV extracted from the EDC spectra (bottom inset) where two clear peaks can be distinguished. Similar to the splitting in the top valence band, we predict this band to be split largely due to spin-orbit coupling and only partially by interlayer interaction.

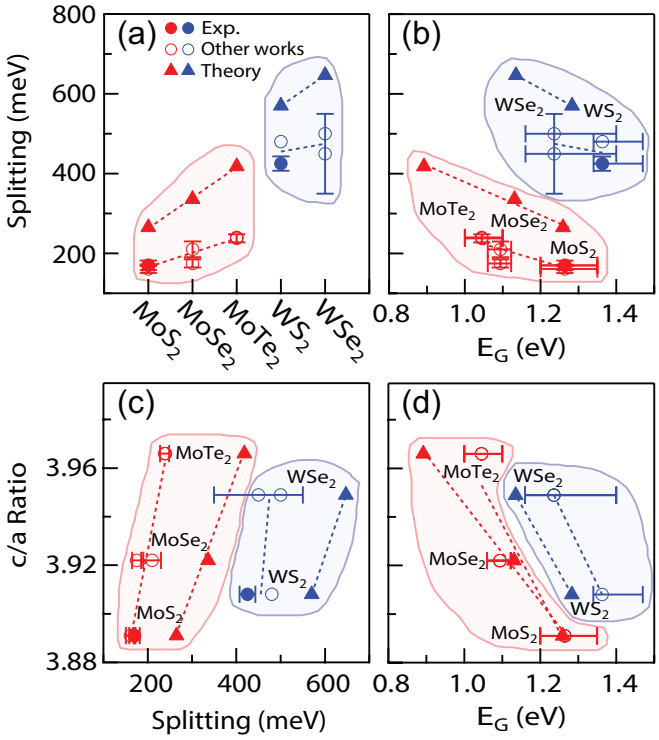

FIG. 4. **(a)** Magnitude of valence band splitting at the $\overline{K}$ point for bulk MoS_2[9,29], $MoSe_2$[29,32], $MoTe_2$[29,33], WS_2[6], and WSe_2[34,35]. **(b)** Magnitude of the splitting vs. band gap (E_G) for bulk MoS_2[29,36–38], $MoSe_2$[29,36–39], $MoTe_2$[29,38], WS_2[36,37,40], and WSe_2[36,37,39,41]. **(c, d)** Ratio of out-of-plane to in-plane lattice constant ($\frac{c}{a}$)[29,42] vs. magnitude of valence band splitting (c) and band gap (d). The dashed lines are guides to the eye indicating the different trends for compounds containing molybdenum (red) and those containing tungsten (blue). The trends are further subdivided between experimental (circles) and theoretical (triangles) data. For all plots, filled (open) symbols represent data from this (other) work(s).

C. Relationship between Band Gap and Spin-Orbit Splitting

Figure 4(a) shows the magnitude of valence band splitting for bulk MoS_2, WS_2, and other bulk TMDs. The molybdenum- and tungsten-based TMDs are ordered separately from left to right with increasing molecular mass. For a given transition metal, the magnitude of the splitting increases as molecular mass increases. These trends are shown by the dashed lines and can be explained as a consequence of the larger intrinsic spin-orbit coupling of the successively heavier atoms. The same general trend is obtained from HSE hybrid functional calculations (triangles), although the splitting appears to be approximately 100 meV larger. Figure 4(c) shows the ratio of out-of-plane to in-plane lattice constant ($\frac{c}{a}$) versus the magnitude of valence band splitting. Similar to the

molecular mass trend, we observe that for a given transition metal, the magnitude of splitting increases with increasing $\frac{c}{a}$ ratio; however, our calculations indicate that although this trend holds across a range of TMDs, it does not hold for individual TMDs.

In addition to the valence band splitting, the band gap plays a key role when considering TMDs for use in spintronics/valleytronics devices. Figure 4(b) shows the magnitude of valence band splitting versus band gap (E_G) for bulk MoS_2, WS_2, and other bulk TMDs. For a given transition metal, the band gap of bulk TMDs decreases with increasing valence band splitting. The same trend is observed as a function of molecular mass in that the band gap decreases with increasing molecular mass. Again, this trend is seen for both experimental and theoretical data even though the magnitude of the splitting for each TMD is calculated to be approximately 100 meV larger than the corresponding experimental values. Figure 4(d) shows the ratio of out-of-plane to in-plane lattice constant versus band gap. It too follows the same trend as molecular mass and valence band splitting in that the band gap decreases with increasing $\frac{c}{a}$ ratio. This strong relationship between the band gap, the valence band splitting, and $\frac{c}{a}$ ratio would help guide the search for suitable TMDs targeted at specific applications.

D. Conclusions

We have presented in-depth high-resolution ARPES studies of the electronic band structure of bulk MoS_2 and WS_2 together with detailed first-principles computations. We have shown that the valence band splitting in bulk WS_2 is primarily due to spin-orbit coupling and not interlayer interaction, resolving previous debates on their relative role. These results strengthen the connection between bulk and monolayer TMDs as the splitting in the monolayer limit is due entirely to spin-orbit coupling. We have shown how the magnitude of this splitting changes for various TMDs and how it correlates with molecular mass, $\frac{c}{a}$ ratio, and band gap. These results provide important new information on how to control these parameters in TMDs and for the development of TMD-based devices in the fields of spintronics and valleytronics.

ACKNOWLEDGMENTS

We thank C. Hwang, C. L. Smallwood, and G. Affeldt for useful discussions. The ARPES work was supported by the sp2 Program at Lawrence Berkeley National Laboratory, funded by the U.S. Department of Energy, Office of Science, Office of Basic Energy Sciences, Materials Sciences and Engineering Division, under Contract No. DE-AC02-05CH11231. The Advanced Light Source is supported by the Director, Office of Science, Office of Basic Energy Sciences, of the U.S. Department of Energy under Contract No. DE-AC02-05CH11231.

The electronic structure calculations at Northeastern University were supported by the US Department of Energy (DOE), Office of Science, Basic Energy Sciences grant number DE-FG02-07ER46352 (core research), and benefited from Northeastern University's Advanced Scientific Computation Center (ASCC), the NERSC supercomputing center through DOE grant number DE-AC02-05CH11231, and support (applications to layered materials) from the DOE EFRC: Center for the Computational Design of Functional Layered Materials (CCDM) under DE-SC0012575. TRC and HTJ are supported by the National Science Council and Academia Sinica, Taiwan. H.L. acknowledges the Singapore National Research Foundation for support under NRF Award No. NRF-NRFF2013-03. We also thank NCHC, CINC-NTU, and NCTS, Taiwan for technical support.

* To whom correspondence should be addressed. Email: alanzara@lbl.gov

[1] Q. H. Wang, K. Kalantar-Zadeh, A. Kis, J. N. Coleman, and M. S. Strano, Nat Nano **7**, 699 (2012).
[2] Z. Y. Zhu, Y. C. Cheng, and U. Schwingenschlögl, Phys. Rev. B **84**, 153402 (2011).
[3] T. Cao, G. Wang, W. Han, H. Ye, C. Zhu, J. Shi, Q. Niu, P. Tan, E. Wang, B. Liu, and J. Feng, Nat Commun **3**, 887 (2012).
[4] D. Xiao, G.-B. Liu, W. Feng, X. Xu, and W. Yao, Phys. Rev. Lett. **108**, 196802 (2012).
[5] H. Zeng, J. Dai, W. Yao, D. Xiao, and X. Cui, Nat Nano **7**, 490 (2012).
[6] A. Klein, S. Tiefenbacher, V. Eyert, C. Pettenkofer, and W. Jaegermann, Phys. Rev. B **64**, 205416 (2001).
[7] A. Molina-Sánchez, D. Sangalli, K. Hummer, A. Marini, and L. Wirtz, Phys. Rev. B **88**, 045412 (2013).
[8] N. Alidoust, G. Bian, S.-Y. Xu, R. Sankar, M. Neupane, C. Liu, I. Belopolski, D.-X. Qu, J. D. Denlinger, F.-C. Chou, and M. Z. Hasan, Nat Commun **5**, (2014).
[9] T. Eknapakul, P. D. C. King, M. Asakawa, P. Buaphet, R.-H. He, S.-K. Mo, H. Takagi, K. M. Shen, F. Baumberger, T. Sasagawa, S. Jungthawan, and W. Meevasana, *Nano Letters*, Nano Lett. **14**, 1312 (2014).
[10] W. Jin, P.-C. Yeh, N. Zaki, D. Zhang, J. T. Sadowski, A. Al-Mahboob, A. M. van der Zande, D. A. Chenet, J. I. Dadap, I. P. Herman, P. Sutter, J. Hone, and R. M. Osgood, Phys. Rev. Lett. **111**, 106801 (2013).
[11] S. K. Mahatha, K. D. Patel, and K. S. R. Menon, Journal of Physics: Condensed Matter **24**, 475504 (2012).
[12] S. K. Mahatha and K. S. R. Menon, Journal of Physics: Condensed Matter **24**, 305502 (2012).
[13] S. K. Mahatha and K. S. R. Menon, Journal of Physics: Condensed Matter **25**, 115501 (2013).
[14] R. Suzuki, M. Sakano, Y. J. Zhang, R. Akashi, D. Morikawa, A. Harasawa, K. Yaji, K. Kuroda, K. Miyamoto, T. Okuda, K. Ishizaka, R. Arita, and Y. Iwasa, Nat Nano **9**, 611 (2014).

[15] A. Damascelli, Z. Hussain, and Z.-X. Shen, Rev. Mod. Phys. **75**, 473 (2003).
[16] P. E. Blöchl, Phys. Rev. B **50**, 17953 (1994).
[17] G. Kresse and D. Joubert, Phys. Rev. B **59**, 1758 (1999).
[18] G. Kresse and J. Hafner, Phys. Rev. B **48**, 13115 (1993).
[19] G. Kresse and J. Furthmüller, Computational Materials Science **6**, 15 (1996).
[20] G. Kresse and J. Furthmüller, Phys. Rev. B **54**, 11169 (1996).
[21] J. P. Perdew, K. Burke, and M. Ernzerhof, Phys. Rev. Lett. **77**, 3865 (1996).
[22] J. Heyd, G. E. Scuseria, and M. Ernzerhof, The Journal of Chemical Physics **118**, 8207 (2003).
[23] J. Heyd, G. E. Scuseria, and M. Ernzerhof, The Journal of Chemical Physics **124**, 219906 (2006).
[24] A. Bansil and M. Lindroos, Phys. Rev. Lett. **83**, 5154 (1999); S. Sahrakorpi, M. Lindroos, R. S. Markiewicz, and A. Bansil, Phys. Rev. Lett. **95**, 157601 (2005); A. Bansil, M. Lindroos, S. Sahrakorpi, and R. S. Markiewicz, Phys. Rev. B **71**, 012503 (2005).
[25] H. Rostami, A. G. Moghaddam, and R. Asgari, Phys. Rev. B **88**, 085440 (2013).
[26] A. Kormányos, V. Zólyomi, N. D. Drummond, P. Rakyta, G. Burkard, and V. I. Fal'ko, Phys. Rev. B **88**, 045416 (2013).
[27] F. J. Himpsel, *Advances in Physics*, Advances in Physics **32**, 1 (1983).
[28] S. Hüfner, *Photoelectron Spectroscopy: Principles and Applications*, 3rd ed. (Springer Berlin Heidelberg, 2003).
[29] T. Böker, R. Severin, A. Müller, C. Janowitz, R. Manzke, D. Voß, P. Krüger, A. Mazur, and J. Pollmann, Phys. Rev. B **64**, 235305 (2001).
[30] K. Fives, I. T. McGovern, R. McGrath, R. Cimino, G. Hughes, A. McKinley, and G. Thornton, Journal of Physics: Condensed Matter **4**, 5639 (1992).
[31] L. F. Mattheiss, Phys. Rev. B **8**, 3719 (1973).
[32] R. Coehoorn, C. Haas, J. Dijkstra, C. J. F. Flipse, R. A. de Groot, and A. Wold, Phys. Rev. B **35**, 6195 (1987).
[33] T. Böker, A. Müller, J. Augustin, C. Janowitz, and R. Manzke, Phys. Rev. B **60**, 4675 (1999).
[34] S.-W. Yu, T. Lischke, R. David, N. Mller, U. Heinzmann, C. Pettenkofer, A. Klein, A. Perlov, E. Krasovskii, W. Schattke, and J. Braun, Journal of Electron Spectroscopy and Related Phenomena **101103**, 449 (1999).
[35] T. Finteis, M. Hengsberger, T. Straub, K. Fauth, R. Claessen, P. Auer, P. Steiner, S. Hüfner, P. Blaha, M. Vögt, M. Lux-Steiner, and E. Bucher, Phys. Rev. B **55**, 10400 (1997).
[36] K. K. Kam and B. A. Parkinson, *The Journal of Physical Chemistry*, J. Phys. Chem. **86**, 463 (1982).
[37] A. Aruchamy, *Photoelectrochemistry and Photovoltaics of Layered Semiconductors*, Physics and Chemistry of Materials with Low-Dimensional Structures (Springer Netherlands, 1992).
[38] L. Gmelin, *Gmelin Handbook of Inorganic and Organometallic Chemistry. Mo - Molybdenum. Supplement Vol. B 7, 8, 9.* (Springer, 1992).
[39] K. K. Kam, C. L. Chang, and D. W. Lynch, Journal of Physics C: Solid State Physics **17**, 4031 (1984).
[40] D. Braga, I. Gutiérrez Lezama, H. Berger, and A. F. Morpurgo, *Nano Letters*, Nano Lett. **12**, 5218 (2012).
[41] M. Traving, M. Boehme, L. Kipp, M. Skibowski, F. Starrost, E. E. Krasovskii, A. Perlov, and W. Schattke, Phys. Rev. B **55**, 10392 (1997).
[42] W. Schutte, J. De Boer, and F. Jellinek, Journal of Solid State Chemistry **70**, 207 (1987).